Synthesis of TiO2/SBA-15 Nanocomposites by Hydrolysis of Organometallic Ti Precursors for Photocatalytic NO Abatement

Ons El Atti, Julie Hot, Katia Fajerwerg, Christian Lorber, Bénédicte Lebeau, Andrey Ryzhikov, Myrtil Kahn, Vincent Collière, Yannick Coppel, Nicolas Ratel-Ramond, et al.

inorganics

MDPI

Article

Synthesis of TiO_2/SBA-15 Nanocomposites by Hydrolysis of Organometallic Ti Precursors for Photocatalytic NO Abatement

Ons El Atti [1,2], Julie Hot [2,*], Katia Fajerwerg [1,*], Christian Lorber [1], Bénédicte Lebeau [3,4], Andrey Ryzhikov [3,4], Myrtil Kahn [1], Vincent Collière [1], Yannick Coppel [1], Nicolas Ratel-Ramond [5], Philippe Ménini [6] and Pierre Fau [5,*]

1 Laboratoire de Chimie de Coordination, CNRS, UPR 8241, 205 Route de Narbonne, 31077 Toulouse, CEDEX 4, France; ons.elatti@lcc-toulouse.fr (O.E.A.); christian.lorber@lcc-toulouse.fr (C.L.); myrtil.kahn@lcc-toulouse.fr (M.K.); vincent.colliere@lcc-toulouse.fr (V.C.); yannick.coppel@lcc-toulouse.fr (Y.C.)
2 Laboratoire Matériaux et Durabilité des Constructions, INSA/UPS Génie Civil, 135 Avenue de Rangueil, 31077 Toulouse, CEDEX 4, France
3 Université de Haute-Alsace, CNRS, Institut de Science des Matériaux de Mulhouse (IS2M), UMR 7361, Axe Matériaux à Porosité Contrôlée (MPC), 68093 Mulhouse, CEDEX, France; benedicte.lebeau@uha.fr (B.L.); andrey.ryzhikov@uha.fr (A.R.)
4 Université de Strasbourg, 67000 Strasbourg, France
5 Laboratoire de Physique et Chimie des Nano-Objets, UMR 5215, INSA/CNRS/Université de Toulouse, 135 Avenue de Rangueil, 31077 Toulouse, CEDEX 4, France; nicolas.ratel-ramond@insa-toulouse.fr
6 Laboratoire d'Analyse et d'Architecture des Systèmes, CNRS, UPR 8001, 7, Avenue du Colonel Roche, 31031 Toulouse, CEDEX 4, France; menini@laas.fr
* Correspondence: hot@insa-toulouse.fr (J.H.); katia.fajerwerg@lcc-toulouse.fr (K.F.); pfau@insa-toulouse.fr (P.F.)

Abstract: The development of advanced photocatalysts for air pollution removal is essential to improve indoor air quality. TiO_2/mesoporous silica SBA-15 nanocomposites were synthesized using an organometallic decoration method, which leverages the high reactivity of Ti precursors to be hydrolyzed on the surface water groups of silica supports. Both lab-made Ti(III) amidinate and commercial Ti(IV) amino precursors were utilized to react with water-rich SBA-15, obtained through a hydration process. The hydrated SBA-15 and the TiO_2/SBA-15 nanocomposites were characterized using TGA, FTIR, ^1H and ^{29}Si NMR, TEM, SEM, N_2 physisorption, XRD, and WAXS. This one-step TiO_2 decoration method achieved a loading of up to 51.5 wt.% of approximately 9 nm anatase particles on the SBA-15 surface. This structuring provided excellent accessibility of TiO_2 particles for photocatalytic applications under pollutant gas and UV-A light exposure. The combination with the high specific surface area of SBA-15 resulted in the efficient degradation of 400 ppb of NO pollutant gas. Due to synergistic effects, the best nanocomposite in this study demonstrated a NO abatement performance of 4.0% per used mg of TiO_2, which is 40% more efficient than the reference photocatalytic material TiO_2 P-25.

Keywords: mesoporous silica; titanium(III) amidinate precursor; TiO_2 nanoparticles; photocatalysis; NO degradation; air quality

Citation: El Atti, O.; Hot, J.; Fajerwerg, K.; Lorber, C.; Lebeau, B.; Ryzhikov, A.; Kahn, M.; Collière, V.; Coppel, Y.; Ratel-Ramond, N.; et al. Synthesis of TiO_2/SBA-15 Nanocomposites by Hydrolysis of Organometallic Ti Precursors for Photocatalytic NO Abatement. *Inorganics* **2024**, *12*, 183. https://doi.org/10.3390/inorganics12070183

Academic Editors: Torben R. Jensen and Roberto Nisticò

Received: 23 May 2024
Revised: 26 June 2024
Accepted: 26 June 2024
Published: 29 June 2024

1. Introduction

Indoor air pollution is a major societal concern in our industrial societies. Indeed, the toxic NO_x ($NO + NO_2$) compounds present in ambient air caused by human activities (e.g., road traffic, industrial plants, and fossil energy combustion) [1] are an environmental threat to human health. In particular, the WHO (World Health Organization) recently revised the air quality guidelines of NO_2 to lower thresholds (from 40 $\mu g/m^3$ in 2005 to 10 $\mu g/m^3$ in 2021 for long-term exposure and from 200 to 25 $\mu g/m^3$ for short-term exposure) [2].

Photocatalysis driven by metal oxide semiconductors has been employed for decades to oxidize and mineralize atmospheric pollutants and reduce the overall pollution levels of NO_x, either in outdoor or indoor conditions [3]. This method relies on the ability of a photocatalytic semiconducting oxide (SCO), such as zinc oxide (ZnO) or titanium dioxide (TiO_2), to promote, under ambient air and solar light exposure, electron/hole pairs that conduce to the formation of free radicals involved in pollutant degradation reactions [4,5]. One of the most studied materials applied in this field is TiO_2, particularly the now archetypical Evonik P-25, which contains a mixture of both anatase (around 80 wt.%) and the high-temperature rutile phase [6,7]. Although the presence of the most photocatalytically active anatase phase is a mandatory requirement, some other physico-chemical parameters can be tuned to enhance the photocatalytic properties of this material. Two parameters are of particular importance to achieve improved photocatalyst properties. First, the specific surface of the SCO has to be increased to allow higher adsorption of pollutant species on its surface. This is generally achieved through the use of nanosized metal oxides, where the surface-to-volume ratio is maximized [8,9]. However, downsizing the particle size in excess can be counterproductive for catalysis if the crystalline domains of the SCO become too small [10]. Indeed, the recombination rate of electron/hole pairs in the SCO is largely driven by the density of point defect in the structure of the material, and highly disordered systems, or quasi-amorphous structures, exhibit low electron/hole pair lifetime due to fast recombination effects [11].

The optimized material for photocatalysis should, therefore, be the result of a compromise between low dimensionality, associated with high specific surface levels, and large crystalline domains where a low recombination rate of excitons is achieved. This delicate balance is difficult to reach with the bare TiO_2 compound only, but one of the possible strategies to overcome this problem is to associate a high specific surface material directly in strong interaction with a well-crystallized TiO_2 anatase phase [12]. A close interface between materials involved in photocatalytic nanocomposites is also a key parameter in reducing the charge carriers' recombination due to surface defects [13,14]. Indeed, SBA-15 is a well-known mesoporous silica material (mesopore size from 3 to 6 nm large) exhibiting a very high specific surface (up to 1000 m^2/g) due to its structuration [15]. Thanks to its porous structure, SBA-15 has been used as an efficient NO_x physisorption material in surface photovoltage (SPV) devices for NO_x gas sensing [16]. SBA-15 is also a material of choice that has already been studied as catalyst support for selective catalytic reduction (SCR) of NO_x found in oxygen-rich exhaust gases at high temperatures [17,18]. The combination of porous SBA-15, which has efficient adsorption properties for gaseous or liquid species, with the photocatalytically active TiO_2 semiconductor has been proposed due to the interesting expected synergism within this hybrid material [8,19–23]. Different chemical protocols are suggested for synthesizing this composite according to the interest of having or not the SCO located inside, outside (or both locations) the pores of the silica matrix. In a one-step protocol, colloidal TiO_2 nanocrystals (prepared from Ti(IV) isopropoxide) are mixed together with the molecular precursors used to build the porous silica matrix (tetraethyl orthosilicate and triblock copolymer Pluronic P123) and followed by an hydrothermal annealing at around 373 K [24]. This technique leads to the efficient incorporation of atomic titanium into the silica matrix and very small TiO_2 particles (mean size 7 nm) within the pores of the SBA-15. From the photocatalysis point of view, these low-crystallinity TiO_2 particles may not be suitable for enabling a low recombination rate of photo-excited charge carriers. Another method that is often employed is the SBA-15, which is a hard template that can be decorated in a second step with TiO_2 prepared from the solution impregnation of a Ti precursor. Landau [25,26] has described a method called CSD (chemical solution decomposition) where a Ti(IV) alkoxide precursor [$Ti(OnBu)_4$)] is maintained inside the pores of the SAB-15 matrix in an autoclave under pressure. After thermal decomposition, the TiO_2 loading is up to 30 wt.% for one run and can be doubled if the procedure is repeated. In that case, the TiO_2 particles are exclusively located in the mesopores of the silica matrix. Several other examples in the literature describe the use

of Ti(IV) precursor for the decoration of mesoporous silica matrixes [19,21,22,27–29]. One important parameter for mastering the size of the TiO_2 nanoparticles is the use of a high-reactivity precursor in order to facilitate the nucleation and growth of nanocrystals under mild conditions [22,30]. In this study, we have prepared a rather unusual precursor based on a Ti(III) amidinate composition [31] that should offer higher reactivity than the usual Ti(IV) ones. This precursor has been used for the first time to decorate hydrated SBA-15 to yield TiO_x nanoparticles located within and outside the mesoporous silica grains. Our chemical process exploits the high reactivity of this type of organometallic precursor toward hydroxyl groups and water molecules adsorbed on silica surface, to directly generate either a crystalline or amorphous metal oxide phase [32–34]. The same procedure was used with a less reactive Ti(IV) precursor (tetrakis(ethylmethylamido)titanium). The two different hybrid nanocomposites have been characterized and their photocatalytic performances were compared for 400 ppb NO abatement under UV-A exposure in humidified air. The use of Ti(III) precursor with hydrated SBA-15 allowed to prepare a photocatalytic material showing a 40% improvement in NO degradation compared to bare P-25 photocatalyst. This result highlights the importance of synergetic mechanisms (specific surface of the matrix and crystalline structure of TiO_2) for photocatalysis reactions and the key role of the metal precursor to yield nanomaterials with optimized performances.

2. Results and Discussion

2.1. SBA-15 Hydration Methods and Characterization

Our team has previously developed a technique that takes advantage of the presence of molecular water on nanostructured supports on which metalorganic precursors react locally to give rise to the growth of nanosized metal oxide particles [32–34]. It is, therefore, important to master and maximize the amount of water in SBA-15 to allow the reaction with the metalorganic precursor to occur. Two methods have been set up in order to control the hydration of the SBA-15 surface. The first method (method A), described by Y. Belmoujahid [35], consists of placing the silica powder in a closed glass vessel containing water saturated with NaCl salt at room temperature (RT) and allowing a constant relative humidity of 75% RH. The water intake saturation in SBA-15 is obtained after around 4 h.

The second method (method B) is rather straightforward and consists of dispersing the silica powder into distilled water placed in a closed glass vessel and letting it boil under reflux at 100 °C for 2 h [36].

The amount of water (wt.%) in the SBA-15 samples was measured with TGA analysis after they were dried for 1 h under a primary vacuum at RT (Figure 1). The water present in the "as-received" SBA-15 powder was evacuated at around 80 °C and corresponded to 8.5% of the total weight. The sample treated with hydration method A (saturated NaCl solution) contained 23.8 wt.% of water, whereas the sample obtained by method B (boiling water at reflux) contained 55 wt.% of water at the same temperature.

The FTIR analyses of the different silica powders confirm this evolution (Figure S1). The siloxane (–Si–O–Si–) band appears as a broad strong peak centered at 1082 cm^{-1}. The bands at 3426 and 1610 cm^{-1} are attributed to the stretching and bending vibrations of the hydroxyl groups and the adsorbed water molecules, respectively. The structural bands of the mesoporous silica are not modified by the adsorption of water.

There are only a few differences between the FTIR spectra of the SBA-15 as-received and that hydrated by method A. Conversely, the spectrum of the sample treated with method B exhibits a higher intensity of the band at 1610 cm^{-1}. The higher loading of water in the sample treated with hydration method B should be more adapted to the next step, where the hydrolysis of the organometallic precursor may lead to the generation of TiO_x nanoparticles on SBA-15.

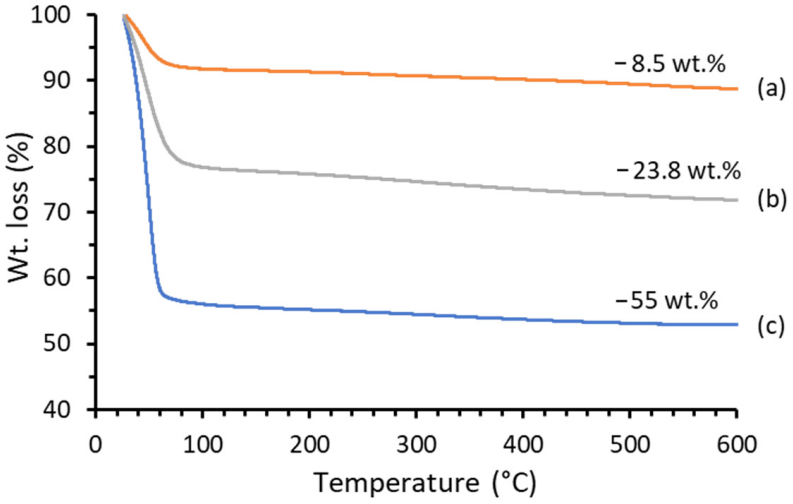

Figure 1. TGA analysis of SBA-15 powders according to hydration methods. (**a**) As-received; (**b**) exposed to air atmosphere with 75% RH for 4 h (method A); and (**c**) soaked in boiling water for 2 h (method B).

Figure 2 shows the ^{1}H NMR MAS (magic angle spinning) spectra of mesoporous SBA-15 silica in the solid state according to the different hydration methods. This figure shows a predominant signal in the region around 4.8 ppm (4.92, 4.99, and 4.71 ppm for the SBA-15 as-received, in method A, and in method B, respectively). This resonance is typical of water molecules in weak interaction with the surface of silica. Part of this signal may also be associated with OH surface groups where their H are rapidly exchanged with those of water. A higher-frequency chemical shift indicates a greater proportion of physisorbed water molecules and/or of hydroxyl OH surface groups, whereas a lower-frequency shift indicates the formation of larger free-water clusters. Their relative populations also have an impact on the linewidth of the resonances because the water in the clusters has greater local mobility than physisorbed molecules and OH groups, leading to sharper resonances for the former. The ^{1}H spectra show that the initial silica already contains a significant amount of water. Hydration method A leads to a slightly higher proportion of physisorbed water and/or OH surface groups. The use of boiling water (method B) leads to the incorporation of a large quantity of free-water clusters and possibly a reduction in the amount of OH surface groups.

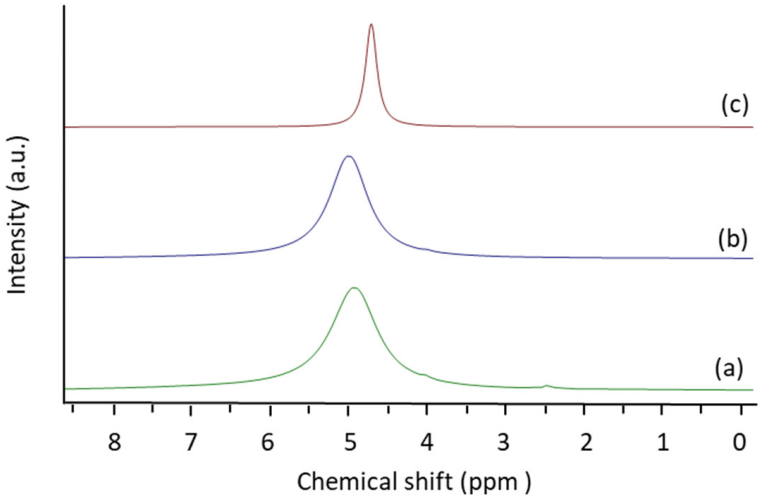

Figure 2. ^{1}H NMR MAS spectra of SBA-15 powders according to hydration methods. (**a**) As-received; (**b**) exposed to air with 75% RH for 4 h (method A); and (**c**) soaked in boiling water for 2 h (method B).

The ^{29}Si MAS NMR spectra (Figure S2) are characterized by three signals typical of Q^4 framework silica sites ($(SiO)_4Si$) (at ~−111 ppm), Q^3 silanol sites ($(SiO)_3$–Si-OH) (at ~−101 ppm) and Q^2 ($(SiO)_2$–(Si-$(OH)_2$) species (at ~−92 ppm). The relative intensity of Q^3 and Q^2 resonances increases in the ^{29}Si CPMAS NMR (Figure S3) compared to MAS experiments as a result of the greater transfer of magnetization from neighboring H than for Q^4. As with ^{1}H NMR, the ^{29}Si NMR spectra of the as-received and hydrated SBA-15 are very close (Figures S2 and S3 green and blue spectra). On the other hand, the spectra of silica hydrated in boiling water (method B) show some differences (Figures S2 and S3 red spectra), with a higher relative proportion of Q^4. The population decrease of Q^2 for the sample prepared with method B is slightly lower than for Q^3 (Figure S2). Low-frequency displacement is also observed in the sample treated with method B and is greater for Q^4 (1.6 ppm in CPMAS and 1.0 ppm in MAS) than for Q^3 (0.6 ppm in CPMAS) and Q^2 (~0.2 ppm in CPMAS). These results indicate a slight but undoubtful modification of the SBA-15 surface in the presence of boiling water, with a lower proportion of OH on the surface. Therefore, the exposition of silica to boiling water leads to the formation of Si–O–Si bonds by dehydration condensation between the hydroxyl groups themselves.

Small-angle XRD pattern and N_2 sorption isotherms of the SBA-15-based materials according to the different hydration methods are reported in Figures S4 and S5, respectively. The corresponding textural properties are presented in Table 1.

Table 1. Textural properties of the different SBA-15 samples.

SBA-15 Sample	S_{BET} (m^2/g)	V_{micro} (cm^3/g)	V_{meso} (cm^3/g)	D_p (nm)
As-received SBA-15	1041	0.16	0.99	6.2
(SBA-15)/A	721	0.08	0.77	6.2
(SBA-15)/B	470	0.04	0.81	7.2

S_{BET} is the specific surface area obtained using the BET model, V_{micro} is the microporous volume extrapolated from the t-plots, $V_{meso} = V_{tot} - V_{micro}$ is the mesopore volume where V_{tot} is the total pore volume obtained at $P/P_0 = 0.9$, and D_p is the mean pore diameter obtained using the BdB model on the desorption branch.

Small-angle XRD patterns of SBA-15 samples show three diffraction peaks (100), (110), and (200) at the same position, which are characteristic of the 2D hexagonal pore (with P6mm hexagonal symmetry typical for SBA-15 mesoporous materials) with the same unit cell a_{hex} of 10.6 nm. No significant evolution of the structure of the silica was noticed, regardless of the hydration treatments used. The same observation was also confirmed by the absence of any change in the microstructure of the different SBA-15 revealed by SEM observations (Figure S6).

Whatever the hydration method, the SBA-15 isotherms are all of type I and IV according to the IUPAC classification [37]. As a result, the as-received SBA-15 material has a high specific surface area (S_{BET} = 1041 m^2/g) and large pore volume (V = 1.15 cm^3/g, V meso + V micro) of 6.2 nm diameter. The SBA-15 synthesized in these conditions simultaneously exhibits mesopores and connections between the main mesopores walls through micropores [38]. It is noteworthy that the hydration method particularly influences the microporous volume (pore size < 2 nm). Indeed, the latter decreases when the amount of water increases, particularly with hydration method B (Table 1, Figure 1). In this case, V_{micro} has decreased by a factor of four compared to the as-received SBA-15 sample. The other textural parameters (V_{meso} and D_p) were less influenced by the hydration method used. The results strongly suggest that hydration treatments induce a phenomenon of silica dissolution/redeposition condensation within micropores, as reported by Galarneau et al. [39]. For the sample hydrated with method B, D_p increased from 6.2 to 7.2 nm, which was due to a decrease in the wall thickness because the unit cell a_{hex} is the same, indicating the same pore-to-pore distance. This evolution is in good agreement with ^{29}Si NMR, which indicates the condensation of hydroxyl groups upon hydration with method B and the formation of more Si–O–Si bonds.

2.2. Bare TiO_2 Powder Syntheses

The synthesis of TiO_x-yH_2O nanopowders was obtained by the controlled hydrolysis under an argon atmosphere of a metalorganic Ti precursor dissolved in an organic solvent (Figure S7). In this procedure, moisture slowly diffuses from the argon gas phase into the organic solvent containing the metalorganic precursor and induces the breaking of nitrogen to metal bonds to eventually produce metal oxide nanoparticles [40]. For the purpose of this study, we tested two different precursors with distinct titanium oxidation numbers. The tetrakis(ethylmethylamido)titanium (TEMAT; see **1** in Scheme 1) is commonly used in the atomic layer deposition (ALD) technique for TiO_2 films [28,41] and demonstrates a Ti center with an oxidation state of IV. In addition, an even more reactive metalorganic precursor for water has been envisaged. We synthesized and studied the hydrolysis in an organic solution of the (N-N′ diisopropylacetamidinato) Ti (III) precursor (Ti-Amd; see **2** in Scheme 1). The presence of a reduced oxidation number for the Ti center is expected to bring a better reactivity of the compound to water. The hydrolysis process, set up under an argon atmosphere at RT, is achieved through the slow diffusion of water from the gas phase into the organic solvent reacting with the Ti precursor, as described in Scheme 1. According to the reaction, 2 molar equivalents of water are necessary for a stoichiometric reaction. In the experimental conditions, an amount of 4 molar equivalents of water is employed in order to saturate the gas phase with water vapor and ensure the full hydrolysis of the dissolved precursors. In these conditions, the hydrolysis reaction takes place over two days.

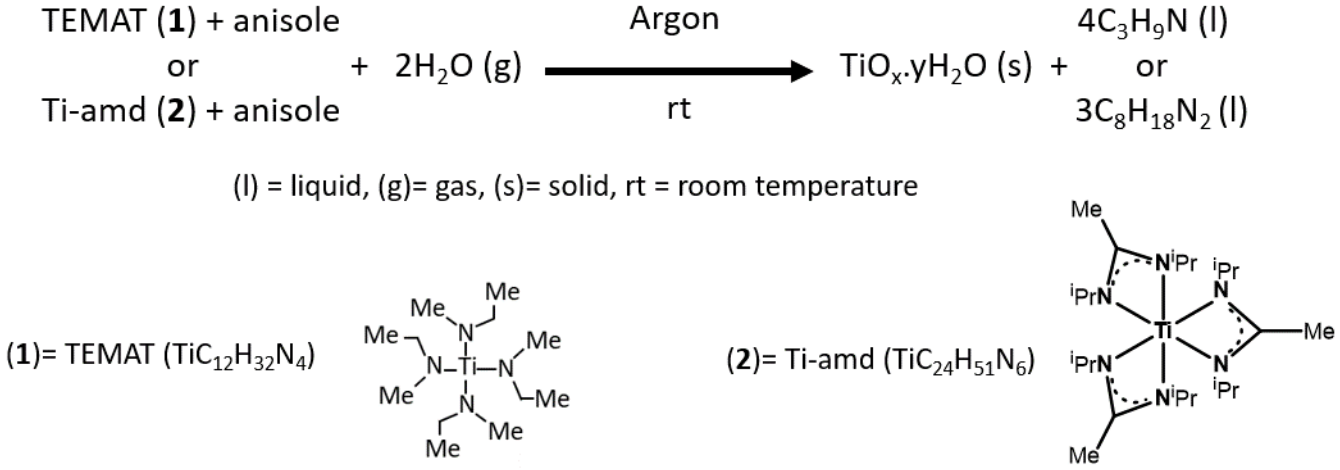

Scheme 1. Hydrolysis reaction of precursor **1** or **2** with a stoichiometric amount of water.

The samples are characterized by wide-angle X-ray scattering (WAXS), a very sensitive technique to determine the local structure of materials with very small crystalline domains (Figure 3). Whatever the precursor composition **1** or **2**, after calcination at 150 °C, the samples have no discernible crystalline domains and correspond to barely amorphous structures (Figure 3a). The pair distribution function (PDF) of the sample obtained from precursor **2** and calcined at 350 °C shows the very first coherence domains corresponding to a crystalline phase (Figure 3b). The structures of TiO_2 anatase (COD 7206075) and TiO_2 brookite (COD 9004140) were refined against the PDF obtained from the WAXS measurement of this sample (Figure 3d,e). Refinement results show that the local structure ($r < 10$ Å) is comparable to that of brookite (Figure 3d), while the average structure ($r > 10$ Å) is close to anatase (Figure 3e). The size of the coherent crystal domains calculated for spherical grains corresponds to a diameter of ca. 3.6 nm. Reversely, the oxide sample obtained from **1** still remains amorphous at this temperature.

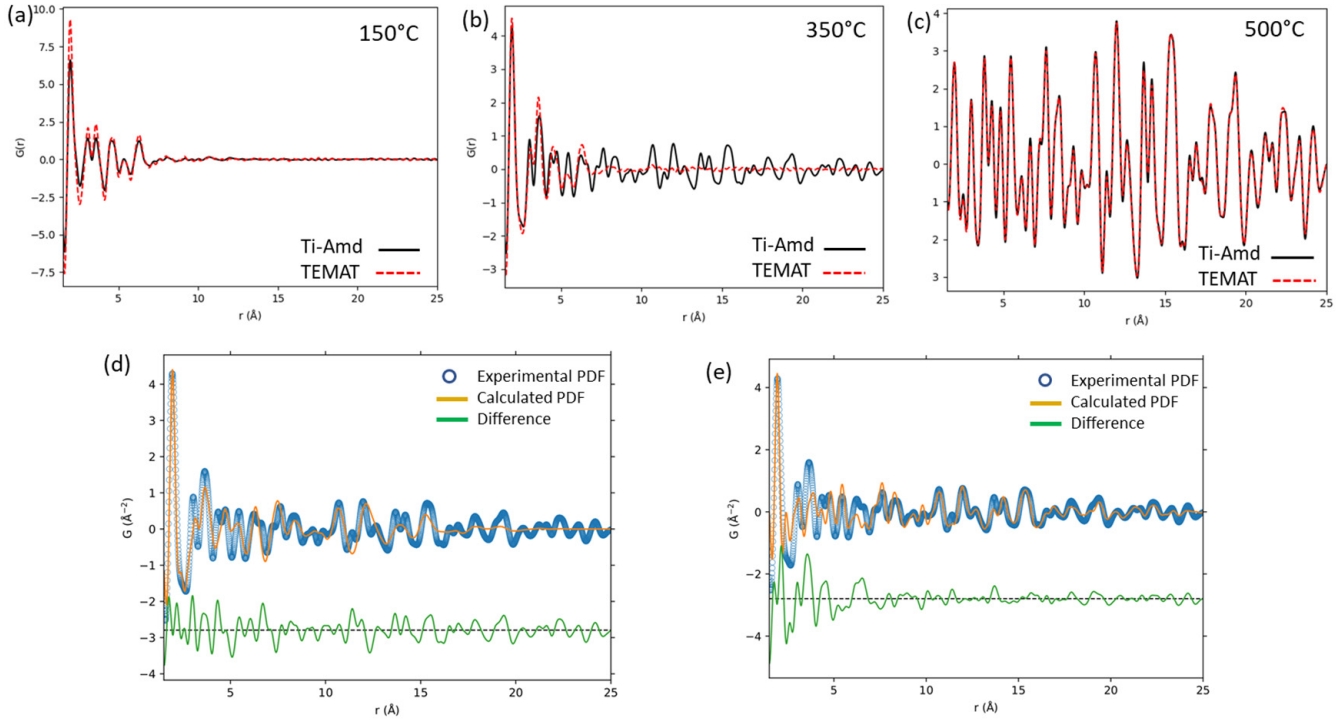

Figure 3. Comparison of PDF obtained from WAXS measurement of TiOx powders from TEMAT (**1**, red dotted line) and Ti-Amd (**2**, plain black line) precursors according to the calcination temperature at: (**a**) 150 °C, (**b**) 350 °C, and (**c**) 500 °C. Refinement of the pair distribution function obtained on TiO_2-amd calcinated at 350 °C with (**d**) brookite and (**e**) anatase structures.

This result clearly shows the higher reactivity of **2** toward hydrolysis, giving rise to an easier growth of crystalline domains at the moderate temperature of 350 °C.

As the calcination temperature increases (500 °C), both samples prepared with TiO_2/Ti-amd or TiO_2/TEMAT unambiguously show the anatase structure of TiO_2, as shown in Figures 3c and S8. According to PDF analysis, TiO_2/TEMAT exhibits coherent domains of 17.5 nm (±2.3 nm), whereas TiO_2/Ti-Amd has a slightly higher crystallite size of 19.8 nm (±2.8 nm), which is consistent with the earlier presence of the very first crystalline domains obtained at 350 °C with this precursor. The presence of the anatase phase after calcination at 500 °C is also confirmed by X-ray diffraction analysis of the different powders (Figure S9). According to the Scherrer equation applied on the (101) peak measured at 2 theta 25.5°, the crystallite size is around 18.4 nm and 21.0 nm for **1** and **2**, respectively.

Figure S10a,c shows the TEM images of the TiO_x-yH_2O powders obtained after hydrolysis of precursors **1** and **2** at RT. The powders have a rather ill-defined microstructure that may be formed by the agglomeration of amorphous particles. Calcination of the as-prepared samples has been performed to remove the water molecules and allow the crystallization of the TiO_2 phase. After calcination at 350 °C, there is no change in the structure of TiO_x grains obtained from **1** (Figure S10b), whereas a nano-structuration (ca. 4 nm grain size, determined on around 100 particles) already appears for the sample prepared with **2** (Figure S10d). After calcination at 500 °C under air, the structuration of the powder is clearly nanocrystalline for the two samples where similar nanosized grain size of ca. 13.5 nm (σ = 3.6 nm) and 13.1 nm (σ = 3.9 nm) are measured for TiO_2 obtained from **1** and **2**, respectively (Figure 4).

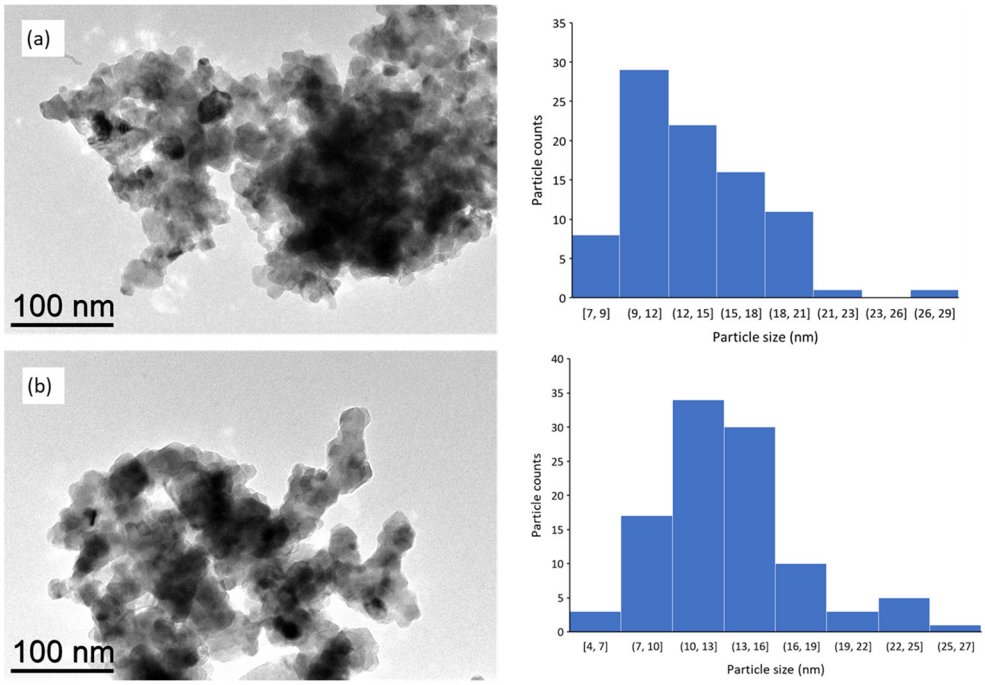

Figure 4. TEM images (left) and corresponding histograms of particle size distribution (right) for TiO_2 powders (determined by ImageJ software (v1.54j) on around 100 particles) after calcination at 500 °C from the hydrolysis of (**a**) TEMAT (**1**) and (**b**) Ti-Amd (**2**).

2.3. Synthesis of TiO_2/SBA-15 Nanocomposites

The decoration of SBA-15 with TiO_2 is performed only on the silica samples prepared with the hydration method B because it leads to a higher amount of water in the silica structure. Indeed, our strategy is to maximize the loading of TiO_2 on SBA-15 by using the hydrated sample that contains a higher amount of adsorbed water.

The mass of the hydrated SBA-15 in our experimental protocol is 200 mg and, since it contains 55 wt.% water (Figure 1), this corresponds to 110 mg of water (i.e., 6 mmol) and 90 mg of SiO_2 per sample. We use an amount of 1.3 mmol of Ti precursor **1** or **2** to react with the hydrated SBA-15, which corresponds to 4.6 molar equivalent of water relative to titanium. Therefore there is a large excess of water compared to the employed Ti precursor and similar to the ratio used for the synthesis of bare TiO_x powders. This excess of water (a stoichiometric amount of 2 molar equivalents according to Scheme 1) is necessary to ensure the complete hydrolysis of the titanium precursor on the silica surface. Assuming the hydrolysis reaction is complete, 1.3 mmol of TiO_2 (62 mg of Ti, 103 mg of TiO_2) will form on the silica, which corresponds to a theoretical mass ratio of Ti equal to 32% (or a mass ratio of 51.5% for TiO_2).

The ICP-MS analyses of the two nanocomposite samples prepared with precursors **1** and **2** are presented in Table 2.

Table 2. ICP-MS analyses of Ti content present inside the TiO_2/SBA-15 nanocomposites obtained from **1** and **2** and calcined at 500 °C.

Precursor	Theoretical Ti Content (wt.%)	ICP Measured Ti Content (wt.%)
TEMAT (**1**)	32	30.09 30.27 Mean: 30.18
Ti-Amd (**2**)	32	31.94 31.17 Mean: 31.55

Interestingly, the experimental amounts of Ti in TiO_2/SBA-15 samples obtained from precursors **1** and **2** (30.2 and 31.5 wt.%, respectively) are very close to the theoretical value previously calculated. This result indicates that, whatever the composition of the Ti precursor, the hydrolysis process is very efficient and leads to the total transformation of the precursor on the silica matrix surface.

Low magnification (×500) SEM images of the nanocomposites calcined at 500 °C are shown in Figure S11. They reveal that the TiO_2 aggregates are exclusively linked to the silica blocks and are distributed on the silica matrix surface.

Figure 5 shows the high magnification SEM image (×5000) of the nanocomposites acquired in the chemical contrast mode (back-scattered electrons). The images confirm that the TiO_2 nanoparticles form aggregated structures over the silica matrix. However, although it appears homogeneous at low magnification (Figure S11), the structuration at high magnification reveals a rather erratic dispersion of TiO_2 aggregated nanoparticles on the porous silica. Some areas of SBA-15 bundles appear to be devoid of TiO_2 particles, while in other locations, TiO_2 nanoparticles are clustered together. This TiO_2 dispersion over the silica matrix is the same for the two Ti precursors studied. In addition, no free TiO_2 aggregate is located apart from the SBA-15 matrix. A SEM-EDS analysis (Figure 6) of the different components of the nanocomposites confirms this particular repartition of TiO_2 nanoparticles over the SBA-15 support.

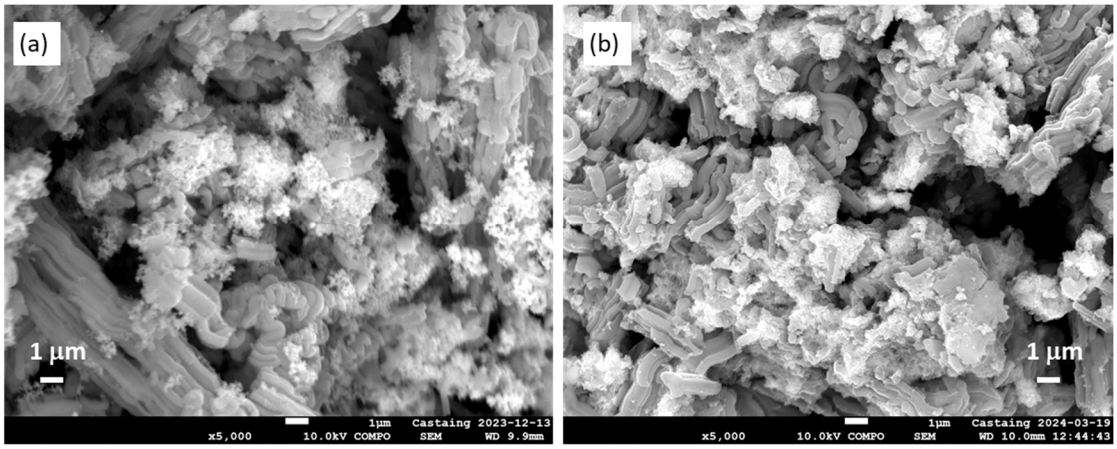

Figure 5. SEM images of TiO_2/SBA-15 calcined at 500 °C and prepared with (**a**) TEMAT (**1**) and (**b**) Ti-Amd (**2**). The images are in chemical contrast mode (back-scattered electrons). The brighter spots on the image correspond to an element with a higher atomic number and indicate the presence of Ti. Magnification is ×5000.

TiO_2 nanoparticles are concentrated in specific zones of the silica matrix. There are locations where the silica matrix is not decorated with TiO_2 whereas the photocatalytic oxide is concentrated into agglomerated structures. This peculiar repartition is very different from what we have previously observed on the decoration of WO_3-$2H_2O$ nanoplatelets with ZnO nanoparticles by using a similar hydrolysis method. In the former case, ZnO appears as a very homogeneous nanostructured layer distributed all over the surface of the WO_3-$2H_2O$ support [33]. This result was achieved thanks to the availability of one of the structural water molecules present in the support to hydrolyze the Zn precursor. In the case of the SBA-15 support, it seems that the water added by the boiling process is not homogeneously distributed over the silica. Instead, water-rich areas, such as clusters or droplets of water, could be randomly distributed over the SBA-15 surface. This assumption is also supported by the ^{1}H MAS NMR analyses that reveal the presence of water clusters in the sample hydrated by method B (boiling water). The Ti precursor in contact with these water reservoirs reacts to locally produce a high density of TiO_x-yH_2O structures. The interesting point is that these water reservoirs remain tightly linked to the substrate because all the TiO_x structures are attached to the silica support in a similar way. This

mechanism is supported by TEM imaging of the nanocomposites (Figure 7). In these images, the TiO_2 nanoparticles appear irregularly dispersed on the silica surface and do not form a continuous layer. Similar TiO_2 grapes are observed for the nanocomposites prepared with precursor **1** or **2**. This analysis confirms that despite the aggregated structure of TiO_2 nanoparticles, they are mainly present on the surface of SBA-15 grains and not dispersed homogeneously into the pores (Figure 7c,d).

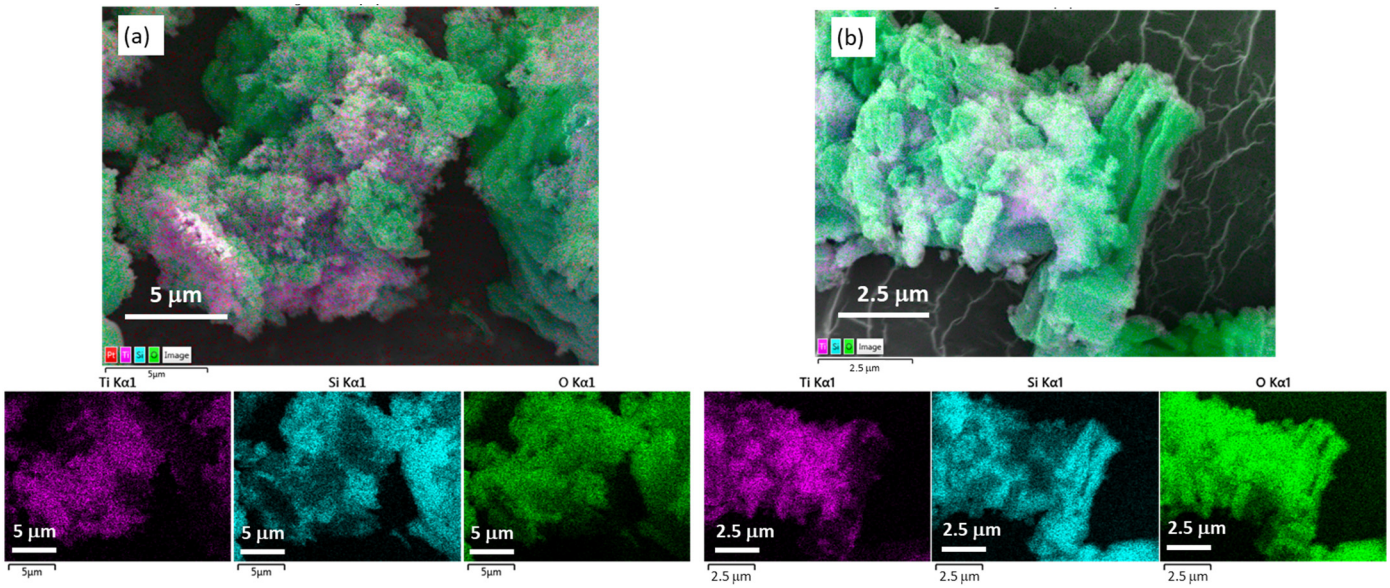

Figure 6. SEM images of TiO_2/SBA-15 prepared with (**a**) TEMAT (**1**) (top) and images in artificial color corresponding to the EDS chemical mapping of elements Ti, Si, and O from the sample (bottom); and (**b**) Ti-Amd (**2**) (top) and EDS chemical mapping for Ti, Si, and O (bottom). Ti atoms are shown in pink, Si atoms are shown in blue, and O atoms are shown in green. A flash platinum layer is deposited on the sample in order to enhance its electrical conductivity and improve the image quality (Pt, red dots displayed uniformly on the image). Magnification is ×5000 for (**a**) and ×10,000 for (**b**).

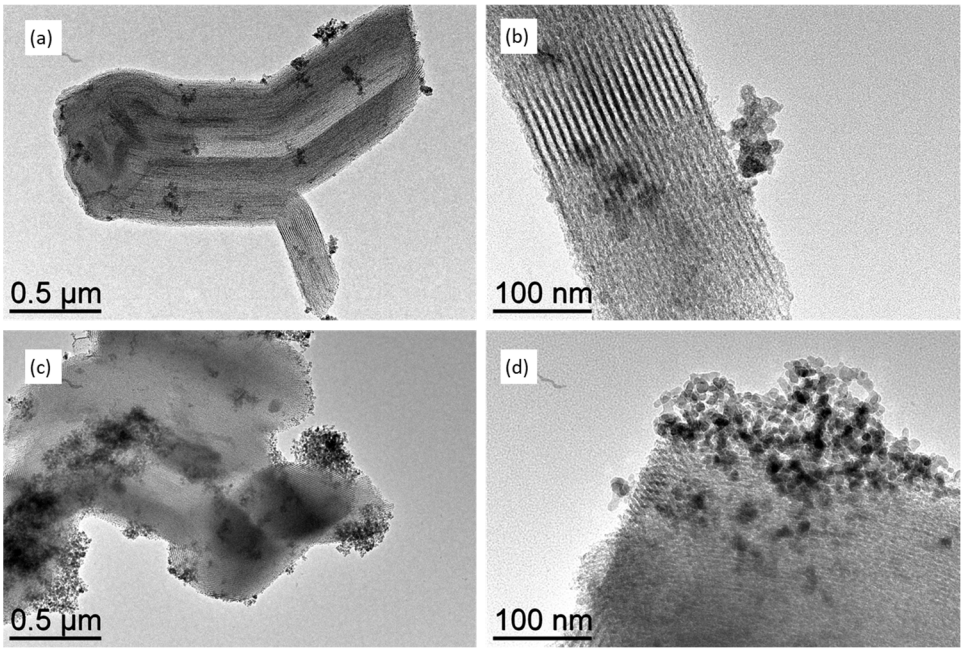

Figure 7. TEM images of TiO_2/SBA-15 nanocomposites obtained from hydrolysis of TEMAT (**1**) (**a**) magnification ×10,000, (**b**) magnification ×100,000, and from hydrolysis of Ti-Amd (**2**) (**c**) magnification ×10,000, (**d**) magnification ×100,000.

The mean grain size of TiO_2 particles formed on SBA-15 supports is close to 9 nm whatever the employed Ti precursor (9.8 and 9.1 nm for precursor **1** and **2**, respectively). This value is clearly lower than that of bare TiO_2 nanoparticles obtained by hydrolysis in solution, which is close to 13 nm (13.5 and 13.1 nm for precursor **1** and **2**, respectively). This result underlines the important role played by the support in the hydrolysis and growth mechanism of the oxide particles. The growth of TiO_2 crystals occurs mainly at the SBA-15 surface, particularly on the micropores where water clusters are present and not inside the mesopores. The interaction between the silica support and TiO_2 induces the particles' stabilization and their limited size. This low dimensionality of the anatase phase is also evidenced by the XRD diffractograms of the nanocomposites, which show all the peaks relating to the crystalline anatase structure but with rather large half-height peaks that reflect the limited size of the crystalline domains (Figure S12 vs. Figure S9).

The main physico-chemical characteristics of the SBA-15 as-received, TiO_2 oxides, and TiO_2/SBA-15 nanocomposites are summarized in Table 3.

Table 3. Main physico-chemical characteristics of the samples tested for photocatalysis.

Sample	TiO_2 Content (wt.%)	S_{BET} (m^2/g)	TiO_2 Crystal Size (nm)	
			TEM	XRD
TiO_2 P-25	100	50	21.0	31.0
$TiO_{2\ TEMAT}$	100	51	13.5	18.4
$TiO_{2\ Ti\text{-}Amd}$	100	21	13.1	21
As-received SBA-15	-	1041	-	-
SBA-15 $_{hydrated\ B}$	-	470	-	-
$TiO_{2\ TEMAT}$/SBA-15	50.4	297	9.8	11.7
$TiO_{2\ Ti\text{-}Amd}$/SBA-15	52.6	251	9.3	11.9

Based on the previous findings, the decoration of hydrated SB1-15 with TiO_x NPs, prepared from the hydrolysis of Ti-Amd precursor, is schematically depicted in Figure 8.

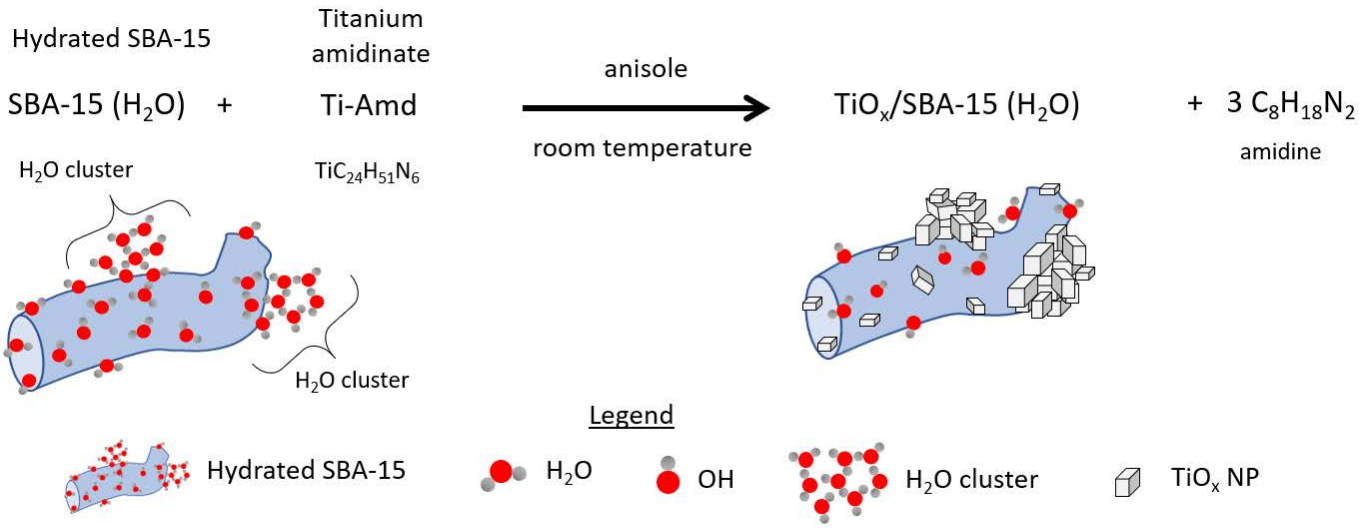

Figure 8. Schematic description of the reaction hydrolysis of Ti-Amd precursor on hydrated SBA-15.

2.4. NO Abatement Tests

NO degradation percentages were calculated from Equation (1) (see Section 3.6 Evaluation of the Photocatalytic Activity) for 20 mg of photocatalytic dispersion applied to the surface of a glass substrate (length × width: 10 × 5 cm^2). The photocatalytic runs were performed on three main types of samples: nanocomposites (TiO_2/SBA-15 obtained from **1** and **2**), bare TiO_2 powders (P-25, TiO_2 powder calcined at 500 °C and obtained from **1** and **2**) and physical mixtures of SBA-15 and TiO_2 powders to assess the role of the

silica matrix. However, the TiO_2/SBA-15 nanocomposites and the SBA-15 mixed with TiO_2 powders are not 100% TiO_2 by weight, unlike the bare oxides (TiO_2 synthesized from **1** and **2**, and TiO_2 P-25). The effective quantity of TiO_2 deposited on the glass surface was therefore considered according to ICP-MS quantification (Table 2) in order to obtain the NO degradation results for the same surface density of TiO_2, i.e., 1 mg of TiO_2 per 50 cm^2 of the substrate surface (0.02 mg/cm^2). The NO degradation results obtained under artificial UV-A light for bare TiO_2, TiO_2/SBA-15 nanocomposites, and SBA-15 physically mixed with bare TiO_2 are shown in Figure 9. The photocatalytic activity of SBA-15 alone was also assessed using the same protocol and found to be equal to zero.

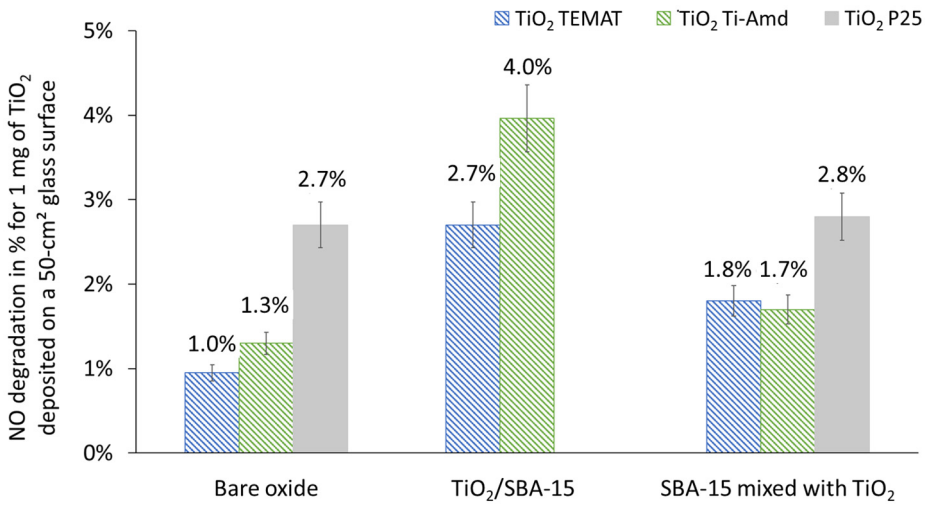

Figure 9. Degradation of NO under UV-A artificial light for the same surface density of TiO_2 (0.02 mg of TiO_2 per cm^2 of glass surface) obtained with bare TiO_2 (TiO_2 synthesized from **1** (TEMAT) and **2** (Ti-Amd) calcined at 500 °C, and TiO_2 P-25), TiO_2/SBA-15 nanocomposites (calcined at 500 °C) and SBA-15 physically mixed with bare TiO_2 oxides (calcined at 500 °C and obtained from **1** and **2**).

For bare oxides, the highest percentage of NO degradation was obtained with TiO_2 P-25 (2.7%). The efficiency of bare oxides obtained from precursors **1** (1%) and **2** (1.3%) was around twice as low. The photocatalytic efficiency of TiO_2 depends on several factors, including crystal structure, crystalline phase, crystallinity, particle size, and surface area, and the balance between these factors determines the overall activity of a given photocatalyst [42]. The air depollution performance of TiO_2 P-25 has been widely reported in the literature and is mainly attributed to the synergistic effect between the anatase and rutile crystalline phases, which reduces photogenerated charge recombination [43,44]. The physico-chemical characterization presented above showed that crystalline anatase was the only phase detected for TiO_2 nanoparticles obtained from **1** and **2** (after calcination at 500 °C, Figure S9), which could explain the lowest activity compared to TiO_2 P-25. Moreover, TiO_2 from **1** had a mean particle size of 13.5 nm and a specific surface area of 51 m^2/g compared with values of 13.1 nm and 21 m^2/g, respectively, for TiO_2 nanoparticles from **2** (Table 3). The two TiO_2 anatase powders prepared in this study demonstrated the same performance for NO abatement (around 1%), which is expected for metal oxides that have similar structural properties.

For the same TiO_2 surface density (1 mg of TiO_2 per 50 cm^2 of substrate surface), the TiO_2/SBA-15 nanocomposites showed similar and even superior performance than TiO_2 P-25. Note that photocatalytic activity is highly dependent on experimental conditions [45], making it difficult to compare the performance of the nanocomposites tested with other materials in the literature. For this reason, we compared the NO degradation percentages obtained with the TiO_2/SBA-15 nanocomposites with those of the reference photocatalyst TiO_2 P-25 tested under the same experimental conditions. The best NO degradation (4.0%) was obtained with $TiO_{2\ Ti\text{-}Amd}$/SBA-15 (around 1.5 times higher than that of TiO_2

P-25), while $TiO_{2\ TEMAT}$/SBA-15 had the same NO degradation percentage than TiO_2 P-25. These results clearly highlighted the following: (1) the advantage of decorating mesoporous SBA-15 silica with TiO_2 nanoparticles compared to the corresponding bare oxides as the performance is increasing by a factor of 3 (1% vs. 2.7% and 1.3% vs. 4.0%), and (2) the higher efficiency of $TiO_{2\ Ti\text{-}Amd}$/SBA-15 compared to bare TiO_2 P-25. The higher photoactivity of TiO_2/SBA-15 nanocomposites compared to bare TiO_2 may be related to three synergistic factors that made NO pollutant molecules more accessible to the active sites and thus improve the photocatalytic reaction: (1) smaller TiO_2 particle size (~12 nm for nanocomposites and ~20 nm for bare oxides, from XRD analysis; Table 3), (2) larger surface area (around 250–300 m^2/g for nanocomposites and around 20–50 m^2/g for bare oxide, Table 3), and (3) well dispersed TiO_2 nanoparticles over the surface of the silica matrix. The positive effect of these factors and the higher photocatalytic activity of mesoporous silica–titania compared to bare TiO_2 were notably highlighted by other authors [46–48].

The last series of results allows us to compare the photocatalytic activity of the physical mixing of TiO_2 powders and SBA-15 to the chemically synthesized nanocomposites (with identical TiO_2/SBA-15 mass ratio). Interestingly, the physical mixing also showed an improvement in NO degradation compared to the corresponding bare TiO_2 powders. However, degradation percentages were lower than those of TiO_2/SBA-15 nanocomposites. A higher UV absorption intensity in the mixed oxides due to the presence of SBA-15 could be responsible for this increase. A stronger UV absorption intensity implies that more TiO_2 particles can be activated by light and, therefore, more photogenerated charges can be promoted, leading to enhanced photocatalytic activity. The role of the received light irradiation on photocatalytic activity was highlighted by several authors in the literature. Notably, Li and Kim [47] partially attributed the higher photo-oxidation of benzene of TiO_2-$xSiO_2$ composites compared to bare titania to greater UV absorption intensity. Alonso-Tellez et al. [49] demonstrated that the higher irradiance received by the UV100 TiO_2 coating and the deeper penetration of light within this coating than in the case of the TiO_2 P-25 coating led to increased conversion and mineralization of the methylethylketone pollutant. This effect is even more pronounced in the case of the chemically prepared nanocomposites of this study, especially for the one prepared with the precursor Ti-Amd.

This suggests a more efficient UV-A sensitization of TiO_2 particles when they are well dispersed and closely attached to the hydrated SBA-15 support, thanks to the use of a highly reactive Ti precursor.

3. Materials and Methods

3.1. Synthesis of SBA-15 Powder

The ordered mesoporous silica SBA-15 was prepared at IS2M (Mulhouse, France) according to the protocol described by Zhao et al. [15]. In a 250 mL polypropylene flask, 4 g of triblock copolymer P123 (Aldrich, Saint Louis, MO, USA) were dissolved in HCl aqueous solution (19.5 mL of 37 wt.% HCl and 127 mL of distilled H_2O). The flask was placed in a water bath at 40 °C with magnetic stirring (500 rpm) for about 3 h to allow a complete dissolution of P123. Then, 8.62 g of Tetraethylorthosilicate TEOS (Aldrich, Saint Louis, MO, USA) were added by maintaining the stirring and the temperature conditions. The molar composition of the gel was 1 TEOS: 0.017 P123: 5.68 HCl: 197 H_2O. The solution was stirred at 40 °C for 24 h and then the bottle was placed without any stirring in an oven for 24 h at 90 °C. The precipitated solid (as-made SBA-15) was recovered by filtration on a Büchner funnel, washed with 200 mL of distilled water, and dried for 48 h at 70 °C. To eliminate the porogen agent (P123) and thus release the porosity of the material, the as-made SBA-15 was calcined under air in a muffle furnace at 300 or 500 °C for 4 h (the heating time from ambient to final temperature was 6 h). The mesoporous silica was hydrated after synthesis in two different ways. The first method (method A) consisted of hydrating the mesoporous silica in a controlled relative humidity atmosphere for 4 h. A 75% relative humidity is created in a closed glass enclosure using an aqueous saturated NaCl (Aldrich) in Milli-Q water solution. The second method (method B) consisted in boiling the mesoporous silica

directly in Milli-Q water (purification system) for 2 h at 100 °C. Typically, around 500 mg of SBA-15 mesoporous silica was brought to reflux in 100 mL of Milli-Q water [36]. Afterward, the water was removed using centrifugation, and the silica paste was dried for 1 h under a vacuum at RT.

3.2. Synthesis of Titanium Tris-Amidinate Precursor

The titanium amidinate (Ti-Amd) precursor was synthesized according to an adaptation of the protocol described by Gordon et al. [31]. All reactions and manipulations were conducted under a nitrogen atmosphere using either a glovebox or a standard Schlenk line technique. The used solvents were dried and collected using a solvent purification system. For the synthesis of the lithium amidinate, a solution of methyllithium (1.6 M in Et_2O, 40 mL, 0.063 mol) in Et_2O was added dropwise using a bromine bulb to a solution of 1,3-diisopropylcarbodiimide (6.9 g, 0.055 mol) in 80 mL of Et_2O at −30 °C. The mixture was warmed to RT and stirred for 4 h. The solvent was then removed under reduced pressure. The resulting white solid was transferred to the glovebox and extracted with pentane (washing three times with 30 mL), then dried under reduced pressure. A solution of the obtained solid in ether was added dropwise to a solution of titanium chloride tetrahydrofuran $TiCl_3.(THF)_3$ (7.8 g, 0.054 mol) in 50 mL of Et_2O. The reaction mixture was stirred for 12 h in the glovebox. The resulting solution was filtered through a pad of Celite® on a glass frit to give a brown solution. The concentration of the filtrate and its cooling to −33 °C in the glovebox afforded a brown solid.

3.3. Synthesis of Bare TiO_2 Powder

TEMAT (tetrakis(ethylmethylamido)titanium IV) was received from Sigma-Aldrich supplier. Ti-Amd (N-N′ diisopropylacetamidinato)titanium III) precursor was prepared in the laboratory according to the protocol described in Section 3.2. The hydrolysis of the organometallic precursors was carried out in a proprietary designed glass reactor (Figure S7), comprising two separated and concentric reservoirs: one containing the dissolved precursor in anisole, and the second placed in the center of the vessel in order to receive the water (4 molar equivalent compared to titanium precursor) introduced from the septum placed above and in the center of the airtight vessel lid. This reactor allowed the slow hydrolysis of the titanium precursor in organic solvent by diffusion of the water from the gas phase to the solvent one, the reaction occurring at the gas-solvent interface. A white TiO_x-yH_2O powder was collected after 2 days, and the powder was purified by washing it in toluene and centrifuged before drying it under a vacuum at RT. The samples were then calcined at various temperatures from 150 to 500 °C for 2 h in air.

3.4. Synthesis of TiO_2/SBA-15 Nanocomposites

The nanocomposites of TiO_2/SBA-15 were synthesized as follows: a volume of 400 µL of Tetrakis(ethylmethylamido)titanium (TEMAT) (99%, STREM, Newburyport, MA, USA), or 613 mg of Ti amidinate precursor, was added to a suspension of 200 mg of hydrated SBA-15 within 12 mL of anisole. Hence, the amount of water introduced in the reaction medium through the hydrated silica corresponds to around 4.6 molar equivalent (i.e., very similar to the amount used to prepare bareTiO_2 by water moisture presented in Section 3.3). The mixture was stirred for 24 h at RT. At the end of the reaction, the resulting solution was centrifuged (15 min, 3000 rpm) and then transferred to the glovebox. The precipitate was repeatedly washed three times with anisole and centrifuged. At the end of the washing procedure, the TiO_x/SBA-15 was dried under a vacuum for 2 h in order to fully remove the anisole solvent. Thermal annealing was performed under air at various temperatures from 150 to 500 °C to achieve fully oxidized and crystallized TiO_2/SBA-15 nanocomposites.

3.5. Characterization Techniques

Thermogravimetric analysis (TGA) was performed using a Setaram thermobalance (Setaram Engineering, Caluire-et-Cuire, France) with a ramp of 10 °C/min in the 30–600 °C range under ambient air.

NMR experiments were recorded on a Bruker Avance 400 III HD spectrometer (Bruker Corp., Billerica, MA, USA) operating at magnetic fields of 9.4 T. Samples were packed into 4 mm zirconia rotors and were rotated at a frequency of 10 kHz at 295 K. ^{1}H MAS were performed with the DEPTH pulse sequence and a recycle delay of 5 s. ^{29}Si MAS were acquired with the UDEFT pulse sequence [50] with a recycle delay of 80 s. Ramped cross-polarization (CP) $^{1}H \rightarrow {}^{29}Si$ MAS spectra were recorded with a recycle delay of 2 s and a contact time of 2 ms. Chemical shifts were referenced to TMS. Fourier transform infra-red spectroscopy (FTIR) spectra were obtained by analyses of SBA-15 powders mixed in a KBr pellet using a Perkin–Elmer 100 spectrometer (Perkin–Elmer, Waltham, MA, USA). The spectra were registered between 4000 and 350 cm^{-1} wavenumbers.

Total scattering (WAXS) measurements were performed on a Malvern Panalytical Empyrean III diffractometer (Malvern, Worcestershire, UK) in transmission geometry, and equipped with a Mo anode (λ = 0.71 Å) and a Galipix3D detector. The maximum reached q value is q_{max} = 16.6 $Å^{-1}$, thus corresponding to a maximum angle of $2\theta_{max}$ = 143°. Powder specimens were placed in 1 mm diameter capillaries. For each specimen measurement, an empty capillary contribution was subtracted. Pair distribution functions (PDF) were extracted using PDFgetX3 software v2.1.2. Least square refinements of experimental PDF were performed using WAXS_toolbox software v1.0 suite [51], based on the diffpy-cmi package [52]. Crystalline structural models of TiO_2 phases were taken from the Crystal Open Database [53]. Powder X-ray diffraction patterns were obtained on a Seifert XRD 3000 TT X-ray diffractometer (Seifert X-ray, Deutschland, Germany), with Cu-Kα radiation, fitted with a diffracted-beam graphite monochromator. Data were collected in the 2θ configuration between an angle of 10 and 70°.

Physisorption measurements were made with the Micromeritics ASAP 2020 analyzer (Micromeritics, Norcross, GA, USA). The samples were degassed at 200 °C under high vacuum for 12 h before analyses. A quantity of 200 mg of powder was used to carry out the measurement. The specific surface area of the samples was determined using the linear part of the Brunauer, Emmet, and Teller (BET) plot, and the pore size was estimated using the desorption branch of the isotherms and the Broekhoff–De Boer (BdB) model. The microporous volume was extrapolated from the linear part of the t-plots.

Transmission electron microscopy (TEM) images were obtained with a Jeol 1400 transmission electron microscope at 120 kV (Jeol Ltd., Akashima, Tokyo, Japan). Field emission scanning electron microscopy (FESEM) images were obtained using a Jeol JSM-6700F microscope operating at 10 kV.

3.6. Evaluation of the Photocatalytic Activity

TiO_2-decorated mesoporous silica powders hydrated using method B with each precursor (**1** for TEMAT and **2** for Ti-Amd at 500 °C) were dispersed in water (10 mg/mL) with sonication for 30 min. Each TiO_2/SBA-15 nanocomposite dispersion was then applied to the surface of the glass substrate (10 cm × 5 cm = 50 cm^2) using a glass pipette. The quantity of the dispersion deposited on the surface was 20 mg for each sample. The same dispersion preparation and deposit protocols were followed for bare oxides (TiO_2 obtained from **1** and **2** at 500 °C as described in Section 3.3, and TiO_2 P-25). Dispersions of SBA-15 mixed (physical mixing) with bare oxides (TiO_2 obtained from **1** and **2**, and TiO_2 P-25) were also prepared and applied to the surface of the glass substrate. The weight percentage of TiO_2 added to these mixtures was chosen to be the same as the one found in TiO_2/SBA-15 nanocomposites (ICP-MS results, Table 2).

Photocatalytic degradation of NO was evaluated using the experimental set-up described by Hot et al. [54] and Castelló Lux et al. [4], to which the reader is kindly referred for a more detailed description of the methodology. It is adapted from standard ISO 22197-

1 [55]. The main points of the protocol to keep in mind as as follows: (1) continuous polluted air (at a flow rate of 1.5 L/min) was injected through the by-pass to check that the desired concentration was reached (400 ppb NO), (2) the polluted air was injected into a borosilicate reactor containing the photocatalytic sample to be tested in the dark for 10 min, (3) the photocatalysis was activated by switching on a UV-A light (Narva LT-T8 Blacklight blue 18 W 073 fluorescent tube) placed above the surface of the sample for 20 min (1 W/m^2 on the sample surface measured with a Gigahertz–Optik radiometer (UV-A detector: UV-3717 model, 315–400 nm; Gigahertz–Optik GmbH, Türkenfeld, Germany), and (4) before the end of the test, the polluted air was returned through the by-pass to check the concentration. Relative humidity and temperature were kept constant at 50% and 20 °C, respectively. The reactor was placed in a light-tight box to isolate the sample from room light and to receive only artificial illumination when the light was switched on. The NO concentration was measured by a chemiluminescence analyzer (model AC32M, Envea SA, Poissy, France).

The photo-oxidation of NO was assessed with Equation (1):

$$\text{NO degradation } (\%) = 100 \times \frac{[\text{NO}]_{\text{initial}} - [\text{NO}]_{\text{final}}}{[\text{NO}]_{\text{initial}}} \quad (1)$$

where $[\text{NO}]_{\text{initial}}$ was the concentration in ppb measured by the analyzer at the exit of the reactor before light activation once the steady state was established, and $[\text{NO}]_{\text{final}}$ was the concentration in ppb measured at the exit of the reactor after the light activation and averaged over the last 10 min.

Photocatalytic tests were conducted on glass samples coated with TiO_2 P-25 oxide, TiO_2/SBA-15 nanocomposite, and SBA-15 mixed with TiO_2 P-25 oxide. Each test was repeated twice.

4. Conclusions

In this paper, we have investigated a novel metalorganic method for the preparation of bare TiO_2 and TiO_2/SBA-15 nanocomposite powders aimed at the photocatalytic abatement of NO pollutant gas (400 ppb). The photocatalytic activity of the different materials prepared in this study is compared, at a laboratory reactor scale, with that of commercial TiO_2 P-25 powder. The mechanical combination of TiO_2 powders with mesoporous SBA-15 silica results in improved photocatalytic abatement of NO compared to bare TiO_2 powders. This improvement is likely due to a more efficient UV diffusion pathway toward the TiO_2 grains. However, chemically prepared TiO_2/SBA-15 nanocomposites demonstrate even higher photocatalytic activity compared with the simple physical mixing of TiO_2 powders with SBA-15 and bare TiO_2 oxides. Specifically, the nanocomposite prepared from Ti-Amd precursor, which is more reactive than TEMAT under hydrolysis conditions, exhibits the best activity for NO abatement with a value of 4.0% (NO abatement/mg of TiO_2 deposited on the glass substrate surface), which represents a 40% increase compared to TiO_2 P-25. Thus, maximizing the interaction and relationship between porous silica and TiO_2 nanoparticles is helpful to achieve a higher synergistic effect for the photocatalytic degradation of NO pollutants. Future work will focus on incorporating Au nanoparticles onto chemically prepared TiO_2/SBA-15 nanocomposites to further enhance the catalytic activity thanks to the plasmonic properties of the noble metal nanoparticles in the visible domain of the spectrum.

Supplementary Materials: The following supporting information can be downloaded at: https://www.mdpi.com/article/10.3390/inorganics12070183/s1, Figure S1: FTIR spectra for SBA-15 according to the hydration pre-treatments; Figure S2: ^{29}Si MAS NMR spectra of SBA-15 powders according to the hydration pre-treatments; Figure S3: ^{29}Si CP-MAS NMR spectra of SBA-15 powders according to the hydration pre-treatments; Figure S4: Small-angle XRD diagrams of SBA-15 powders according to the hydration pre-treatments; Figure S5: N_2 adsorption isotherms of SBA-15 powders according to the hydration pre-treatments; Figure S6: SEM images of SBA-15 powders according to the hydration pre-treatments; Figure S7: Scheme of the glass vessel used for the controlled

hydrolysis of metalorganic precursor in organic solvent under argon; Figure S8: Refinement of anatase structures against PDF obtained on (a) TiO_2-amd and (b) TiO_2-TEMAT after calcination at 500 °C; Figure S9: X-ray diffraction diagrams of TiO_2 powders obtained after annealing at 500 °C under air of precursor (a) Ti-Amd and (b) TEMAT; Figure S10: TEM images of TiO_x powders obtained from hydrolysis of TEMAT (a) as-prepared, (b) calcined at 350 °C under air, and from hydrolysis of Ti-Amd (c) as-prepared, (d) calcined at 350 °C under air. Magnification is ×50,000 for (a,c), and ×100,000 for (b,d); Figure S11: SEM image of TiO_2/SBA15 powders calcined at 500 °C showing the homogeneous repartition of the TiO_2 over the silica matrix in the sample (a,c) TiO_2 obtained from TEMAT hydrolysis (magnification ×500 and ×2000 respectively), (b,d) TiO_2 obtained from Ti-Amd hydrolysis (magnification ×500 and ×5000 respectively); Figure S12: XRD analyses of nanocomposites TiO_2/SBA-15 calcined at 500 °C and (a) prepared from precursor TEMAT, (b) prepared from precursor Ti-Amd.

Author Contributions: O.E.A. carried out the synthesis of oxides and nanocomposites, performed the photocatalytic tests and data analyses, prepared the figures, and wrote the experimental section of the manuscript; J.H. coordinated the joint research, supervised the photocatalytic experiments, wrote the catalysis section, and participated in reviewing the manuscript; K.F. coordinated the joint research, supervised the hydrolysis experiments, conducted data analyses, and participated in reviewing the manuscript; C.L. supervised the metalorganic preparation of Ti-Amd precursor and its characterization; B.L. and A.R. supervised the preparation of SBA-15 material employed for the study, performed the N_2 adsorption experiments and analyses, participated to scientific working meetings; M.K. participated to scientific working meetings; V.C. was in charge of the SEM, SEM-EDS and TEM analyses; Y.C. carried out the NMR experiment and NMR analysis section; N.R.-R. performed the WAXS experiments and analysis section; P.M. participated in scientific working meetings; P.F. coordinated the joint research, supervised the study, the hydrolysis method, and data analyses, wrote the draft, and finalized the manuscript. All authors have read and agreed to the published version of the manuscript.

Funding: The research project DPOLAIR was funded by the Allocation Doctorale Interdisciplinaire (ADI 21) program of the Université Fédérale de Toulouse Midi-Pyrénées (UFTMP) and the Région Occitanie.

Data Availability Statement: The original contributions presented in the study are included in the article/Supplementary Material, further inquiries can be directed to the corresponding author/s.

Acknowledgments: Simon Cayez (LPCNO-INSA) for XRD measures, Stéphane Leblond du Pouy (Centre de micro-caractérisation Castaing, Toulouse, France) for SEM analyses, and Frederic Averseng (Laboratoire de Réactivité de Surface, Sorbonne Université, Paris, France) for EPR discussion.

Conflicts of Interest: The authors declare no conflicts of interest.

References

1. Lorente, A.; Boersma, K.F.; Eskes, H.J.; Veefkind, J.P.; van Geffen, J.H.G.M.; de Zeeuw, M.B.; Denier van der Gon, H.A.C.; Beirle, S.; Krol, M.C. Quantification of nitrogen oxides emissions from build-up of pollution over Paris with TROPOMI. *Sci. Rep.* **2019**, *9*, 20033. [CrossRef] [PubMed]
2. WHO Global Air Quality Guidelines. Available online: https://www.who.int/news-room/questions-and-answers/item/who-global-air-quality-guidelines (accessed on 29 March 2024).
3. Ângelo, J.; Andrade, L.; Madeira, L.M.; Mendes, A. An overview of photocatalysis phenomena applied to NO_x abatement. *J. Environ. Manag.* **2013**, *129*, 522–539. [CrossRef]
4. Castelló Lux, K.; Hot, J.; Fau, P.; Bertron, A.; Kahn, M.L.; Ringot, E.; Fajerwerg, K. Nano-gold decorated ZnO: An alternative photocatalyst promising for NO_x degradation. *Chem. Eng. Sci.* **2023**, *267*, 118377. [CrossRef]
5. Seiss, V.; Thiel, S.; Eichelbaum, M. Preparation and Real World Applications of Titania Composite Materials for Photocatalytic Surface, Air, and Water Purification: State of the Art. *Inorganics* **2022**, *10*, 139. [CrossRef]
6. Uddin, M.J.; Cesano, F.; Chowdhury, A.R.; Trad, T.; Cravanzola, S.; Martra, G.; Mino, L.; Zecchina, A.; Scarano, D. Surface Structure and Phase Composition of TiO_2 P25 Particles After Thermal Treatments and HF Etching. *Front. Mater.* **2020**, *7*, 192. [CrossRef]
7. Qian, R.; Zong, H.; Schneider, J.; Zhou, G.; Zhao, T.; Li, Y.; Yang, J.; Bahnemann, D.W.; Pan, J.H. Charge carrier trapping, recombination and transfer during TiO_2 photocatalysis: An overview. *Catal. Today* **2019**, *335*, 78–90. [CrossRef]
8. Noureen, L.; Wang, Q.; Humayun, M.; Shah, W.A.; Xu, Q.; Wang, X. Recent advances in structural engineering of photocatalysts for environmental remediation. *Environ. Res.* **2023**, *219*, 115084. [CrossRef]

9. Toma, F.L.; Bertrand, G.; Klein, D.; Coddet, C. Photocatalytic removal of nitrogen oxides via titanium dioxide. *Environ. Chem. Lett.* **2004**, *2*, 117–121. [CrossRef]
10. Du, L.; Furube, A.; Yamamoto, K.; Hara, K.; Katoh, R.; Tachiya, M. Plasmon-Induced Charge Separation and Recombination Dynamics in Gold−TiO_2 Nanoparticle Systems: Dependence on TiO_2 Particle Size. *J. Phys. Chem. C* **2009**, *113*, 6454–6462. [CrossRef]
11. Sun, S.; Song, P.; Cui, J.; Liang, S. Amorphous TiO_2 nanostructures: Synthesis, fundamental properties and photocatalytic applications. *Catal. Sci. Technol.* **2019**, *9*, 4198–4215. [CrossRef]
12. MiarAlipour, S.; Friedmann, D.; Scott, J.; Amal, R. TiO_2/porous adsorbents: Recent advances and novel applications. *J. Hazard. Mater.* **2018**, *341*, 404–423. [CrossRef]
13. Jiang, W.; Ji, W.; Au, C.-T. Surface/Interfacial Catalysis of (Metal)/Oxide System: Structure and Performance Control. *ChemCatChem* **2018**, *10*, 2125–2163. [CrossRef]
14. Kumar, S.G.; Rao, K.S.R.K. Comparison of modification strategies towards enhanced charge carrier separation and photocatalytic degradation activity of metal oxide semiconductors (TiO_2, WO_3 and ZnO). *Appl. Surf. Sci.* **2017**, *391*, 124–148. [CrossRef]
15. Zhao, D.; Huo, Q.; Feng, J.; Chmelka, B.F.; Stucky, G.D. Nonionic Triblock and Star Diblock Copolymer and Oligomeric Surfactant Syntheses of Highly Ordered, Hydrothermally Stable, Mesoporous Silica Structures. *J. Am. Chem. Soc.* **1998**, *120*, 6024–6036. [CrossRef]
16. Yamada, T.; Zhou, H.; Uchida, H.; Honma, I.; Katsube, T. Experimental and Theoretical NO_x Physisorption Analyses of Mesoporous Film (SBA-15 and SBA-16) Constructed Surface Photo Voltage (SPV) Sensor. *J. Phys. Chem. B* **2004**, *108*, 13341–13346. [CrossRef]
17. Boutros, M.; Onfroy, T.; Da Costa, P. Mesostructured or Alumina-mesostructured Silica SBA-16 as Potential Support for NO_x Reduction and Ethanol Oxidation. *Catal. Lett.* **2010**, *139*, 50–55. [CrossRef]
18. Bin, F.; Song, C.; Lv, G.; Song, J.; Cao, X.; Pang, H.; Wang, K. Structural Characterization and Selective Catalytic Reduction of Nitrogen Oxides with Ammonia: A Comparison between Co/ZSM-5 and Co/SBA-15. *J. Phys. Chem. C* **2012**, *116*, 26262–26274. [CrossRef]
19. Sharma, M.V.P.; Kumari, V.D.; Subrahmanyam, M. TiO_2 supported over SBA-15: An efficient photocatalyst for the pesticide degradation using solar light. *Chemosphere* **2008**, *73*, 1562–1569. [CrossRef]
20. Acosta-Silva, Y.J.; Nava, R.; Hernandez-Morales, V.; Macias-Sanchez, S.A.; Gomez-Herrera, M.L.; Pawelec, B. Methylene Blue photodegradation over titania-decorated SBA-15. *Appl. Catal. B* **2011**, *110*, 108–117. [CrossRef]
21. Wang, X.-j.; Li, F.-t.; Hao, Y.-j.; Liu, S.-j.; Yang, M.-l. TiO_2/SBA-15 composites prepared using H2TiO3 by hydrothermal method and its photocatalytic activity. *Mater. Lett.* **2013**, *99*, 38–41. [CrossRef]
22. Besancon, M.; Michelin, L.; Josien, L.; Vidal, L.; Assaker, K.; Bonne, M.; Lebeau, B.; Blin, J.-L. Influence of the porous texture of SBA-15 mesoporous silica on the anatase formation in TiO_2-SiO_2 nanocomposites. *New J. Chem.* **2016**, *40*, 4386–4397. [CrossRef]
23. Conceicao, D.S.; Graca, C.A.L.; Ferreira, D.P.; Ferraria, A.M.; Fonseca, I.M.; Botelho do Rego, A.M.; Teixeira, A.C.S.C.; Vieira Ferreira, L.F. Photochemical insights of TiO_2 decorated mesoporous SBA-15 materials and their influence on the photodegradation of organic contaminants. *Microporous Mesoporous Mater.* **2017**, *253*, 203–214. [CrossRef]
24. Araujo, M.M.; Silva, L.K.R.; Sczancoski, J.C.; Orlandi, M.O.; Longo, E.; Santos, A.G.D.; Sa, J.L.S.; Santos, R.S.; Luz, G.E.; Cavalcante, L.S. Anatase TiO_2 nanocrystals anchored at inside of SBA-15 mesopores and their optical behavior. *Appl. Surf. Sci.* **2016**, *389*, 1137–1147. [CrossRef]
25. Vradman, L.; Peer, Y.; Mann-Kiperman, A.; Landau, M.V. Thermal decomposition-precipitation inside the nanoreactors. High loading of W-oxide nanoparticles into the nanotubes of SBA-15. In *Studies in Surface Science and Catalysis*; Park, S.-E., Ryoo, R., Ahn, W.-S., Lee, C.W., Chang, J.-S., Eds.; Elsevier: Amsterdam, The Netherlands, 2003; Volume 146, pp. 121–124.
26. Landau, M.V.; Vradman, L.; Wang, X.; Titelman, L. High loading TiO_2 and ZrO_2 nanocrystals ensembles inside the mesopores of SBA-15: Preparation, texture and stability. *Microporous Mesoporous Mater.* **2005**, *78*, 117–129. [CrossRef]
27. Peza-Ledesma, C.L.; Escamilla-Perea, L.; Nava, R.; Pawelec, B.; Fierro, J.L.G. Supported gold catalysts in SBA-15 modified with TiO_2 for oxidation of carbon monoxide. *Appl. Catal. A Gen.* **2010**, *375*, 37–48. [CrossRef]
28. Ke, W.; Liu, Y.; Wang, X.; Qin, X.; Chen, L.; Palomino, R.M.; Simonovis, J.P.; Lee, I.; Waluyo, I.; Rodriguez, J.A.; et al. Nucleation and Initial Stages of Growth during the Atomic Layer Deposition of Titanium Oxide on Mesoporous Silica. *Nano Lett.* **2020**, *20*, 6884–6890. [CrossRef]
29. Wang, C.-Y.; Shen, K.; Gorte, R.J.; Vohs, J.M. Preparation of SBA-15-Supported Metals by Vapor-Phase Infiltration. *Inorganics* **2022**, *10*, 215. [CrossRef]
30. Garden, J.A.; Pike, S.D. Hydrolysis of organometallic and metal–amide precursors: Synthesis routes to oxo-bridged heterometallic complexes, metal-oxo clusters and metal oxide nanoparticles. *Dalton Trans.* **2018**, *47*, 3638–3662. [CrossRef]
31. Lim, B.S.; Rahtu, A.; Park, J.-S.; Gordon, R.G. Synthesis and Characterization of Volatile, Thermally Stable, Reactive Transition Metal Amidinates. *Inorg. Chem.* **2003**, *42*, 7951–7958. [CrossRef]
32. Cure, J.; Piettre, K.; Coppel, Y.; Beche, E.; Esvan, J.; Colliere, V.; Chaudret, B.; Fau, P. Solution Layer Deposition: A Technique for the Growth of Ultra-Pure Manganese Oxides on Silica at Room Temperature. *Angew. Chem. Int. Ed.* **2016**, *55*, 3027–3030. [CrossRef]

33. Castello Lux, K.; Fajerwerg, K.; Hot, J.; Ringot, E.; Bertron, A.; Collière, V.; Kahn, M.L.; Loridant, S.; Coppel, Y.; Fau, P. Nano-Structuration of WO_3 Nanoleaves by Localized Hydrolysis of an Organometallic Zn Precursor: Application to Photocatalytic NO2 Abatement. *Nanomaterials* **2022**, *12*, 4360. [CrossRef] [PubMed]
34. Jonca, J.; Castello-Lux, K.; Fajerwerg, K.; Kahn, M.L.; Colliere, V.; Menini, P.; Sowka, I.; Fau, P. Gas Sensing Properties of $CuWO_4$@WO_3 n-n Heterojunction Prepared by Direct Hydrolysis of Mesitylcopper (I) on $WO_3{\cdot}2H_2O$ Nanoleaves. *Chemosensors* **2023**, *11*, 495. [CrossRef]
35. Belmoujahid, Y.; Bonne, M.; Scudeller, Y.; Schleich, D.; Grohens, Y.; Lebeau, B. SBA-15 mesoporous silica as a super insulating material. *Eur. Phys. J. Spec. Top.* **2015**, *224*, 1775–1785. [CrossRef]
36. Wang, W.; Song, M. Photocatalytic activity of titania-containing mesoporous SBA-15 silica. *Microporous Mesoporous Mater.* **2006**, *96*, 255–261. [CrossRef]
37. Thommes, M. Physisorption of gases, with special reference to the evaluation of surface area and pore size distribution (IUPAC Technical Report). *Chem. Int.* **2016**, *38*, 25. [CrossRef]
38. Galarneau, A.; Cambon, H.; Di Renzo, F.; Ryoo, R.; Choi, M.; Fajula, F. Microporosity and connections between pores in SBA-15 mesostructured silicas as a function of the temperature of synthesis. *New J. Chem.* **2003**, *27*, 73–79. [CrossRef]
39. Galarneau, A.; Nader, M.; Guenneau, F.; Di Renzo, F.; Gedeon, A. Understanding the Stability in Water of Mesoporous SBA-15 and MCM-41. *J. Phys. Chem. C* **2007**, *111*, 8268–8277. [CrossRef]
40. Amiens, C.; Chaudret, B.; Ciuculescu-Pradines, D.; Collière, V.; Fajerwerg, K.; Fau, P.; Kahn, M.; Maisonnat, A.; Soulantica, K.; Philippot, K. Organometallic approach for the synthesis of nanostructures. *New J. Chem.* **2013**, *37*, 3374–3401. [CrossRef]
41. Niemelä, J.-P.; Marin, G.; Karppinen, M. Titanium dioxide thin films by atomic layer deposition: A review. *Semicond. Sci. Technol.* **2017**, *32*, 093005. [CrossRef]
42. Mamaghani, A.H.; Haghighat, F.; Lee, C.-S. Photocatalytic oxidation technology for indoor environment air purification: The state-of-the-art. *Appl. Catal. B Environ.* **2017**, *203*, 247–269. [CrossRef]
43. Bickley, R.I.; Gonzalez-Carreno, T.; Lees, J.S.; Palmisano, L.; Tilley, R.J.D. A structural investigation of titanium dioxide photocatalysts. *J. Solid State Chem.* **1991**, *92*, 178–190. [CrossRef]
44. Hendrix, A.L.Y.; Yu, Q.; Brouwers, J. Titania-Silica Composites: A Review on the Photocatalytic Activity and Synthesis Methods. *World J. Nano Sci. Eng.* **2015**, *5*, 161–177. [CrossRef]
45. Russell, H.S.; Frederickson, L.B.; Hertel, O.; Ellermann, T.; Jensen, S.S. A Review of Photocatalytic Materials for Urban NO_x Remediation. *Catalysts* **2021**, *11*, 675. [CrossRef]
46. Inada, M.; Enomoto, N.; Hojo, J. Fabrication and structural analysis of mesoporous silica–titania for environmental purification. *Microporous Mesoporous Mater.* **2013**, *182*, 173–177. [CrossRef]
47. Li, Y.; Kim, S.-J. Synthesis and Characterization of Nano titania Particles Embedded in Mesoporous Silica with Both High Photocatalytic Activity and Adsorption Capability. *J. Phys. Chem. B* **2005**, *109*, 12309–12315. [CrossRef] [PubMed]
48. Xu, Y.; Zheng, W.; Liu, W. Enhanced photocatalytic activity of supported TiO_2: Dispersing effect of SiO_2. *J. Photochem. Photobiol. A Chem.* **1999**, *122*, 57–60. [CrossRef]
49. Alonso-Tellez, A.; Masson, R.; Robert, D.; Keller, N.; Keller, V. Comparison of Hombikat UV100 and P25 TiO_2 performance in gas-phase photocatalytic oxidation reactions. *J. Photochem. Photobiol. A Chem.* **2012**, *250*, 58–65. [CrossRef]
50. Duong, N.T.; Trébosc, J.; Lafon, O.; Amoureux, J.-P. Improved sensitivity and quantification for 29Si NMR experiments on solids using UDEFT (Uniform Driven Equilibrium Fourier Transform). *Solid State Nucl. Magn. Reson.* **2019**, *100*, 52–62. [CrossRef] [PubMed]
51. Ratel-Ramond, N. Nicoratel/WAXS_toolbox: PDF-for-nano (v1.0.0-alpha). *Zenodo*, 2024. [CrossRef]
52. Juhás, P.; Farrow, C.L.; Yang, X.; Knox, K.R.; Billinge, S.J. Complex modeling: A strategy and software program for combining multiple information sources to solve ill posed structure and nanostructure inverse problems. *Acta Crystallogr. Sect. A Found. Adv.* **2015**, *71*, 562–568. [CrossRef]
53. Gražulis, S.; Chateigner, D.; Downs, R.T.; Yokochi, A.F.T.; Quirós, M.; Lutterotti, L.; Manakova, E.; Butkus, J.; Moeck, P.; Le Bail, A. Crystallography Open Database—An open-access collection of crystal structures. *J. Appl. Crystallogr.* **2009**, *42*, 726–729. [CrossRef]
54. Hot, J.; Topalov, J.; Ringot, E.; Bertron, A. Investigation on Parameters Affecting the Effectiveness of Photocatalytic Functional Coatings to Degrade NO: TiO_2 Amount on Surface, Illumination, and Substrate Roughness. *Int. J. Photoenergy* **2017**, *2017*, 6241615. [CrossRef]
55. *ISO 22197-1:2016*; Fine Ceramics (Advanced Ceramics, Advanced Technical Ceramics)—Test Method for Air-Purification Performance of Semiconducting Photocatalytic Materials—Part 1: Removal of Nitric Oxide. ISO: Geneva, Switzerland, 2016. Available online: https://www.iso.org/standard/65416.html (accessed on 20 November 2023).